Archaeopteryx feathers and bone chemistry fully revealed via synchrotron imaging

U. Bergmann[a], R. W. Morton[b], P. L. Manning[c,d], W. I. Sellers[e], S. Farrar[f], K. G. Huntley[b], R. A. Wogelius[c,g,1], and P. Larson[c,f]

[a]Stanford Linear Accelerator Center National Accelerator Laboratory, Stanford Synchrotron Radiation Lightsource, Menlo Park, CA 94025; [b]Children of the Middle Waters Institute, Bartlesville, OK, 74003; [c]School of Earth, Atmospheric, and Environmental Sciences, University of Manchester, Manchester, M13 9PL, United Kingdom; [d]Department of Earth and Environmental Sciences, University of Pennsylvania, Philadelphia, PA, 19104; [e]Faculty of Life Sciences, University of Manchester, Manchester, M13 9PT, United Kingdom; [f]Black Hills Institute of Geological Research, Inc., Hill City, SD, 57745; and [g]Williamson Research Centre for Molecular Environmental Science, University of Manchester, Manchester, M13 9PL, United Kingdom

Evolution of flight in maniraptoran dinosaurs is marked by the acquisition of distinct avian characters, such as feathers, as seen in *Archaeopteryx* from the Solnhofen limestone. These rare fossils were pivotal in confirming the dinosauria-avian lineage. One of the key derived avian characters is the possession of feathers, details of which were remarkably preserved in the Lagerstätte environment. These structures were previously simply assumed to be impressions; however, a detailed chemical analysis has, until now, never been completed on any *Archaeopteryx* specimen. Here we present chemical imaging via synchrotron rapid scanning X-ray fluorescence (SRS-XRF) of the Thermopolis *Archaeopteryx*, which shows that portions of the feathers are not impressions but are in fact remnant body fossil structures, maintaining elemental compositions that are completely different from the embedding geological matrix. Our results indicate phosphorous and sulfur retention in soft tissue as well as trace metal (Zn and Cu) retention in bone. Other previously unknown chemical details of *Archaeopteryx* are also revealed in this study including: bone chemistry, taphonomy (fossilization process), and curation artifacts. SRS-XRF represents a major advancement in the study of the life chemistry and fossilization processes of *Archaeopteryx* and other extinct organisms because it is now practical to image the chemistry of large specimens rapidly at concentration levels of parts per million. This technique has wider application to the archaeological, forensic, and biological sciences, enabling the mapping of "unseen" compounds critical to understanding biological structures, modes of preservation, and environmental context.

trace elements | X-ray absorption spectroscopy

Archaeopteryx (1) are rare but occupy a pivotal place in the development of Darwinian evolution because of their possession of both reptilian (jaws with teeth and a long bony tail) and avian (feathered wings) characters (2). The specimen used in this study is considered to be the most complete and best preserved archaeopterygid (3) belonging to the species *A. siemensii* (4). Previous analyses of this fossil have relied upon visual inspection, X-ray computer tomography, scanning electron, and ultraviolet/visible light microscopy. Structural studies have been extensive and strongly indicate that this organism is transitional between dinosaurs and birds; however, detailed chemical analysis has never been performed. Here we apply state-of-the-art synchrotron rapid scanning X-ray fluorescence (SRS-XRF) imaging to this remarkably well-preserved specimen revealing striking and previously unknown details about the chemical preservation of soft tissue, elemental distribution patterns most likely related to the organism's life processes, insights into the chemistry of the fossilization process, and details of curation history. In addition, quantitative chemical analyses and X-ray absorption spectroscopy are presented that not only corroborate the imaging results but also give further details about fossil composition and mode of preservation. We are thus able to obtain key chemical information as to how the remarkable preservation of this critical fossil occurred. New taphonomic details, when combined with the contextual information SRS-XRF provides about the sedimentary matrix, can be used to help explain how this detailed fossil has survived over 150 million years. SRS-XRF thus allows direct study of (*i*) structures that are not apparent in visible light, (*ii*) macronutrient and trace metal distribution patterns in bone and mineralized soft tissue areas related to life processes, and (*iii*) chemical processes of fossilization. SRS-XRF will also enable advances in a wide variety of disciplines, including biomolecule extraction, fraud detection, and assessment of curation damage.

Paleontological Specimen Details

This *Archaeopteryx* is preserved within a matrix of limestone from the Solnhofen region of Bavaria, Germany (3, 4) and was selected because of its remarkable preservation. Housed at the Wyoming Dinosaur Center in Thermopolis (Wyoming, USA), it is hence referred to as the Thermopolis specimen (WDC-CSG-100). Previous study using ultraviolet induced fluorescence photography (3) indicated that the distal left humerus, distal right femur, and proximal right tibiotarsus were restored during preparation.

XRF Imaging

The analysis of XRF spectra has long been known to be a sensitive, quantitative tool for studying elemental compositions of materials (5, 6). Fossil XRF imaging studies on the basis of commercially available devices showed that many specimens are not simply preserved impressions but are actually "chemical fossils" including elemental residue perhaps representing both soft and hard tissues (7, 8). However, these original studies proved too slow to make imaging large fossils practical, because high quality elemental maps took more than 24 hours/cm^2 to acquire.

Intense, collimated, polarized, and tunable X-ray beams produced at synchrotron facilities have made dramatic advances in XRF microimaging possible, and efforts since the landmark work (9) have focused on improving spatial resolution, now achieving 100 nm (10). Recently, emphasis has also been put on enhancing the scanning speed at moderate resolution in order to image large objects, as with the illegible pages of the Archimedes Palimpsest (11–13) and other studies (14, 15). In the SRS-XRF imaging technique developed at the Stanford Synchrotron Radiation Lightsource (SSRL), signals from multiple elements are now read out at intervals of several milliseconds per pixel during bidirectional scans (11, 15). This dramatic reduction of the scan time to

~30 seconds/cm^2 at 100 µm resolution has made the present study possible. Because of the intense nature of the incident synchrotron X-ray beam, imaging is not only rapid enough to be practical for large objects but also can successfully record spatial variation at even lower concentrations of an element than is typically possible with standard electron beam methods; approximately an order of magnitude better sensitivity can be achieved routinely with the current SSRL configuration.

SRS-XRF applied to paleontology makes it possible to simultaneously probe elemental distributions of large organisms and their embedding geological matrix, thus resolving the exchange of material between the organism and the surrounding sediment during fossilization. In analyzing the *Archaeopteryx* via SRS-XRF, we expected to identify and image the chemical remains of soft tissues such as feathers, to characterize, quantify, and image the trace element contents of bone materials and surrounding sediments, and to detect curation artifacts. Interpretation builds on previous imaging studies of geochemical and environmental phenomena, e.g., hydrothermal systems (16), carbonate mineral formation (17–19), and contaminant uptake (20). Determination of (*i*) element exchange between bone and sediment, (*ii*) advective flux through high permeability features, and (*iii*) system oxidation state were of particular importance. In situ analysis of fossil plus matrix was intended to provide information critical not only for understanding life processes of an extinct organism, but also to provide such geochemical information. Results from paleontological studies will also enable better predictions of mass flux in similar environmental systems involving contaminant transport.

SRS-XRF scans were completed at SSRL. One set of scans was taken at 3.15 keV for light elements; scans were repeated at 13.5 keV for heavier elements. Distribution maps of Si, P, S, Cl, Ca, Ba, Mn, Fe, Zn, Cu, Br, and Pb were produced of the entire fossil and surrounding matrix (all maps are presented in Fig. S1). Point analyses were completed along with the elemental maps. Point analyses allow us to apply a concentration scale to the maps and also provide well-constrained measurements of elemental abundances at various points within the specimen and matrix. As with the images, point analyses were made at incident energies of both 3.15 and 13.5 keV. We also completed an X-ray absorption near edge structure (XANES) measurement at the S K edge within the humerus in order to determine the oxidation state of sulfur associated with bone material (in *SI Text*, see *Synchrotron Rapid Scanning X-ray Fluorescence* for further analytical details and *Image Processing for Figures* for image processing information). New details about the original physiology, fossilization process, and curation of the Thermopolis specimen were revealed. First we present findings related to original physiology.

Results

Feather and Bone Chemistry Revealed via Imaging. A comparison of a visible light photo (*Inset*) with a full SRS-XRF map of phosphorous is presented in Fig. 1. Extremely fine detail is apparent in the XRF image. Most striking is that, in addition to the bone material, the chemical remains of the rachises (shafts) from the flight feathers are now revealed: The P distribution is clearly controlled by both bone as well as soft tissue remnant from the original organism. Although phosphatized muscle tissue has been reported from the Solnhofen (21), the phosphorus and sulfur levels responsible for the rachis images presented here do not require the addition of P or S from elsewhere. Indeed, the levels we report for the rachis in Table 1 (310 ppm for P and 65 ppm for S) represent P concentrations well within the documented range of extant feathers (22–26) and S concentrations 3 orders of magnitude lower than S levels reported for extant feathers (27). Thus there is no need to add P and S via geochemical processes to produce these images; in fact, there has been considerable S loss and probably loss of P as well. Furthermore, experimental studies have shown that the feather shaft (rachis) is more resistant to degradation by bacterial enzymes (keratinases) isolated from *Bacillus subtilis* than the barbules (28), and hence the pattern we uncover of only rachises remnant with all smaller fibers removed is consistent with what one would predict on the basis of relative stability of feather components. Hence we conclude that while we cannot rule out phosphatization, the evidence strongly implies that the rachises are at least in part the chemical remains of the original organism.

Imaging also shows that the distribution of zinc is controlled by fossil bone material. This control is clearly shown in Fig. 2, which presents a false color chemical intensity map of a selected region for three elements (calcium, red; zinc, green; manganese, blue). Calcium is the major component of the surrounding limestone matrix. Manganese-rich dendrites indicate inorganic metal precipitation under oxidizing conditions. However, the extremely good correlation between the zinc intensity and the fossil bone locations clearly indicates that zinc is concentrated in the bone. Zinc concentrations in the limestone are low, and there is little evidence for zinc transfer by aqueous fluids in this system. Furthermore, noting that zinc levels are high in the bone material of many extant organisms (e.g., over 100 ppm in black-tailed gulls; see ref. 29) and that zinc has been shown in forensic research to be relatively well-conserved within bone (30), we conclude that the high zinc levels in the *Archaeopteryx* bone have been inherited from the original organism.

XRF point analyses presented in Table 1 support the chemical zoning determined in the imaging scans. (In *SI Text*, see *Synchrotron Rapid Scanning X-ray Fluorescence* for more details on XRF
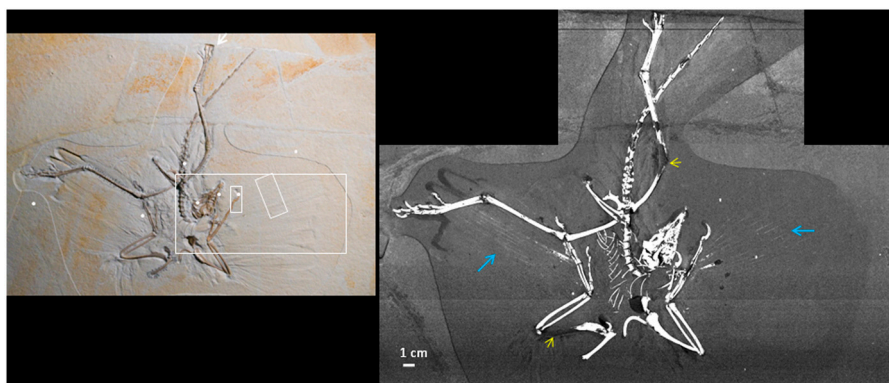

Fig. 1. SRS-XRF map of the phosphorous distribution in the Thermopolis *Archaeopteryx*. This map clearly shows the splay of the rachises from the flight feathers (*Blue Arrows*) and the reconstructed areas (*Yellow Arrows*). The *Inset* shows visible light photograph where, although striking feather impressions exist, the rachises are not discernible. The *Inset* also shows the location of several point analyses (*White Dots*) and regions highlighted for image analysis (*White Rectangles*).

Table 1. XRF point analysis quantification for *Archaeopteryx* and host sedimentary rock

	Vertebra	Tooth	Claw	Skull	Humerus	Rachis	Sed. 1	Sed. 2	Sed. 3	ICP sed.*	Solnhofen lit. values (32, 36)
P	340	42,800	350	38,400	37,890	310	31	4	7	41 (0.01)	200–600
S	270	1,570	270	1,310	1,480	65	110	51	72	3,011 (80)	150–300
Cl	140	51	160	0	26	47	85	51	69		
Ca†	54%	17%	38%	21%	28%	8%	49%	24%	39%		35–39%
Mn	110	15	53	25	na	16	36	25	na	13 (1)	100–300
Fe	2,200	3,100	860	810	610	340	4,860	3,670	3,060	73 (1.6)	1,000–15,000
Ni	5	8	3	7	na	4	7	7	na		
Cu	8	17	5	18	na	8	9	7	na	9 (1.6)	
Zn	13	19	8	49	na	12	22	18	na	22 (2.2)	
As	2	6	3	6	na	3	3	5	na		

All numbers in ppmw except where noted as percent weight.

*ICP-MS (Mn, Fe, Cu, and Zn) and ICP-AES (P and S) analyses were made of a dissolved sediment sample taken from the reverse side of the slab; 2σ errors given in parentheses. (See Fig. S4 for an example point analysis spectrum with fit.)

†Theoretical calcium concentrations in apatite and calcite are 39% and 40% by weight, respectively. All values presented here were calculated (standardless) from fundamental parameters, so the high resulting Ca values for the vertebra and sediment 1 allow us to estimate errors of approximately 30% at the Ca Kα energy. Errors therefore are estimated to be ∼50% of the reported values for elements lighter than Ca, decreasing to ∼25% or less for the higher atomic weight elements. Errors are because of imprecision caused by topographic irregularity, depth heterogeneity, and low count rates (in some cases).

quantification methodology and error estimation, and see *Sediment Analysis* for details of sediment inductively coupled plasma spectrometry [ICP] analyses.) Analysis of the skull, perhaps the thickest bone in the specimen, gives the highest values of Zn, which are double the values in the sedimentary matrix and consistent with the good image contrast in Zn shown in Fig. 2. Mn and Fe levels may be affected by the precipitation of Mn(IV) and Fe(III) oxyhydroxides that are almost certainly postdepositional inorganic precipitates, but high Zn levels are not associated with these inorganic precipitates. Therefore, the high Zn levels in the bone point analyses unequivocally corroborate the scan results. Similarly, phosphorous point levels measured from the rachis are over an order of magnitude greater than values measured in the surrounding sedimentary matrix, strongly supporting the inference that part of the feather chemistry is preserved. A statistical comparison further supports the chemical distributions determined by imaging and point analysis.

Anatomical Correlate Analysis. Anatomical correlates of particular elements revealed within the SRS-XRF images were analyzed to test our conclusions regarding physiological control of element
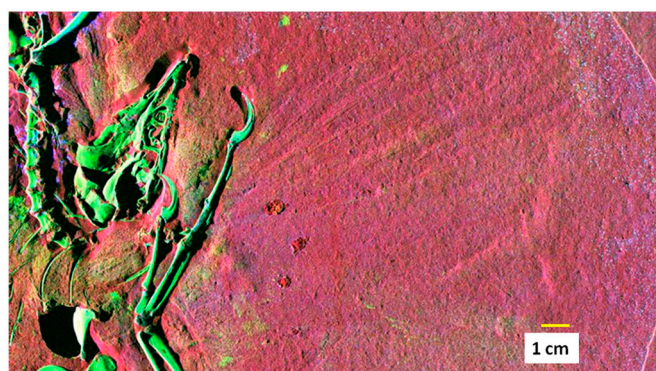

Fig. 2. False color SRS-XRF map of *Archaeopteryx*. Color code is calcium, red; Zn, green; and Mn, blue. Higher intensities correspond to higher concentrations; see Table 1 for concentrations. Host rock is limestone, and hence high calcium surrounds the fossil. Blue flecks on the surface result from the presence of tiny precipitates of Mn(IV) oxide minerals that are ubiquitous along bedding planes and within fractures. There is some zinc associated with the mineral precipitates, but almost all of the Zn inventory in this image is associated with the *Archaeopteryx* bone material. Zinc apparently was present in appreciable concentrations in the original bone (as in many extant organisms) and has been well sequestered within the bone over 150 million years of burial.

distributions by comparison of elemental levels associated with different anatomical structures as shown in Fig. 3. Besides indicating how anatomical features relate to distributions of individual elements, this type of analysis also shows which of the mean values are influenced by the presence of large numbers of zero intensities associated with shadowing so that shadow regions could be masked and ignored during image analysis. For all analyzed elements the statistical distribution within the feathers is similar to that within the slab, consistent with our findings that only trace amounts of material remain in soft tissue regions. For all other anatomical features, all elemental distributions (except Mn) are appreciably different when compared to the slab; Ca is lower than the matrix whereas all other elements are clearly enriched in the bone material. We especially call attention to the graphs showing the high Zn and Cu intensities associated with the skull, claws, postcranial skeleton, and teeth. These again serve to corroborate the high levels determined by point analysis for the skull (see Table 1). Finally, P and S concentrations in the teeth of the *Archaeopteryx* appear to be at their maximum values through statistical image analyses as well as via the point analyses given in Table 1. These comparisons show that (*a*) elemental intensities in the maps represent real chemical heterogeneities in the fossil and can be used as a basis for discussion of elemental variation in the *Archaeopteryx* pre- and postfossilization, and (*b*) elemental analysis consisting of solely a few points must be treated with caution because concentrations may strongly vary even within a single anatomical feature.

To demonstrate the appreciable elemental variation within anatomical structures on a submillimeter scale, detailed sections of elemental maps associated with the manus claw region are shown in Fig. 4. The highest contrast between claw and the surrounding matrix is in the phosphorus channel, and a strong P signal is also seen for a feather calamus in the lower right. Calcium is clearly lower in the bone than the sediment, whereas in contrast Zn, Cu, and S are all more concentrated in the bone relative to the sediment, consistent with the point analyses. Unexpectedly, the elemental maps of the bone in the manus claw are nearly indistinguishable from its keratinous sheath. Another detailed example of elemental variation is given in Fig. 5, which shows part of the feather region rotated so the feather shafts (rachis) are aligned horizontally and all the elemental scans clipped to the 95th percentile to stop them being overwhelmed by bright speckles. The differences in the information content are clear: In particular, the P channel (Fig. 5, *Left*) in this region shows remnants of rachises that could be overlooked in more global segmentation.
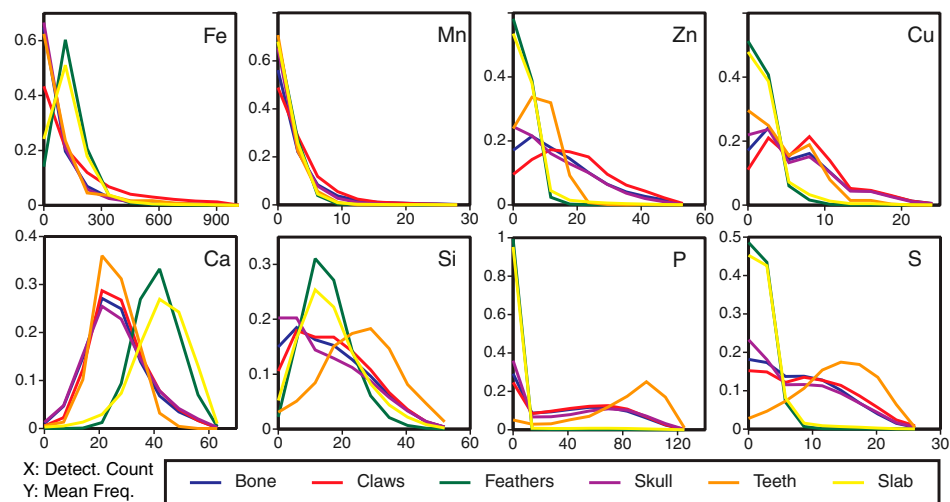
Bergmann et al.

Fig. 3. Detector count distributions assigned to individual anatomical categories for eight elements: Fe, Mn, Zn, Cu, Ca, Si, P, and S. The frequency of pixels giving a detector intensity response is plotted as a function of counts. "Bone" refers to combined areas of postcranial skeleton. (Further method details are in *SI Text* in *Synchrotron Rapid Scanning X-ray Fluorescence*.) For all elements besides Mn, the histolines for *Archaeopteryx* bone, claws, teeth, and skull are clearly different from the embedding sediment slab, showing that a chemical fossil indeed endures. The feather is far less distinct from the sediment, consistent with diminished preservation of soft tissue relative to bone.

Insights to Taphonomy. Comparison to other work supports our conclusion that certain bone trace metals have been conserved. Proton-induced X-ray emission (PIXE) analyses of comparable species (31) show Zn levels in modern bone to be 100–200 ppm and that Zn is essentially conserved over geological time (dinosaur samples ranged from 6 to 500 ppm, mean = 117). Although we show above that Zn is clearly higher in selected *Archaeopteryx* bones than in the host sediment, comparison to modern bone and other fossils (31) does suggest some Zn depletion from *Archaeopteryx* bone. Nonetheless, the skull of *Archaeopteryx* has apparently retained approximately 50% of its original Zn. Other work (31) thus supports our most striking result: that elevated Zn levels associated with the skull and other bones have persisted over geological time and most likely, along with phosphorous and sulfur, are remnants of the original bone chemistry.

Our analyses may also indicate how matrix chemistry influences elemental exchange between the fossil and its environment. Consider that loss of phosphorous relative to calcium typically occurs as bone ages. Initial Ca:P ratios for modern avian and crocodilian bone range from 1.75 to 2.73 (31). In recent PIXE analyses of sixteen dinosaur specimens representing four depositional environments and six genera, all showed some calcium depletion but phosphorous removal was more extensive in most samples (31). Our results follow this trend; however, our maximum P concentration is 4 times lower than even the lowest PIXE result (31), consistent with over 90% P removal. In contrast, Ca removal from some parts of the *Archaeopteryx* is negligible, with depletion percentages as low as 4%. *Archaeopteryx* is hosted

within a high Ca environment, and therefore it is not surprising that Ca depletion of the bone apatite has been minimal. Samples used in the PIXE study (31) were hosted within silica-dominated lithologies, and hence Ca concentrations in pore fluids may have been low, thus favoring Ca depletion. Ca loss might also enhance trace metal uptake, and in fact specimens from elsewhere (31) show Fe and Mn enrichment levels as high as 180,000 and 13,000 ppm, respectively. Fe and Mn levels in the *Archaeopteryx* bone, although higher than typical for modern bone, are nowhere near as high as those reported via PIXE (31). We conclude this is in part because high levels of dissolved Ca in Solnhofen formation fluids suppress Ca-Fe and Ca-Mn exchange.

Phosphorous, however, shows extensive removal compared to Ca in the *Archaeopteryx*, most likely because the Solnhofen has quite low P concentrations. Phosphorous would therefore be low in formation fluids, thus favoring phosphate removal. Phosphorous from *Archaeopteryx* also presented an important added nutrient source for microbial activity. Phosphorous loss from the *Archaeopteryx* and low P levels in the host lithology (600 ppm or lower) are in direct contrast to the high P retention in some of the fossils (180,000 and 160,000 ppm P) and the reported higher host
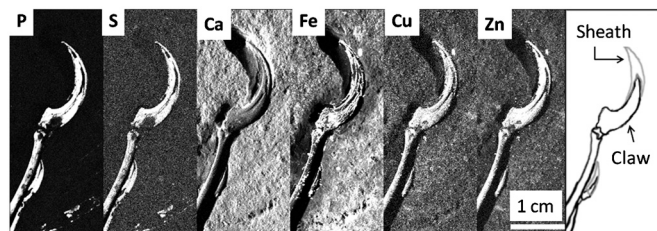

Fig. 4. Detector count maps for P, S, Ca, Fe, Cu, and Zn of the claw region clipped so that white corresponds to the 95th percentile of the overall count distribution. At right for reference is a sketch showing locations of the manus claw and sheath.
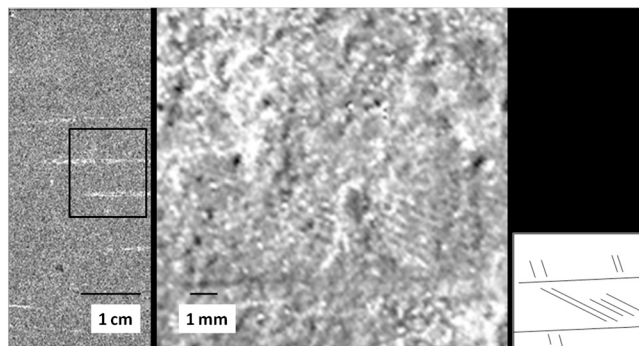

Fig. 5. Phosphorous and iron in the rachis. At left, a detail of the phosphorous map taken from the rachis area indicated in Fig. 2. The box indicates the region exploded in the right image, which is an Fe map of this area showing the extremely fine barb detail evident at moderate magnification. The small sketch at far right indicates fabric of the barb pattern shown in the Fe map (note that more structure is contained in the image than that shown schematically).

GEOLOGY

EVOLUTION

sediment P concentrations of 5,000 ppm pertinent to the PIXE analytical study (31). Therefore sediment chemistry probably served to enhance phosphorous removal but inhibit Ca loss from the *Archaeopteryx* bone and also kept levels of Mn and Fe relatively low in the fossilized bone. Retention of Ca may also have helped immobilize Zn.

In addition to elemental concentrations, oxidation state determination of redox sensitive elements provides critical environmental and taphonomic information. In particular, pyritization of fossil bone is common and indicative of a reducing environment. Because of the many possible oxidation states of sulfur, a XANES spectrum was obtained for sulfur contained within the *Archaeopteryx* humerus (see Fig. S2). This spectrum showed that sulfur in the bone is dominated by sulfate. No reduced iron sulfide minerals are detectable, indicating that subsequent to the reducing conditions pertinent to initial sediment deposition (32) the fossilization environment has been oxidizing for at least part of the specimen's history, as previously suggested because of a lack of organic carbon residue on the feathers of all but one existing *Archaeopteryx* specimens (33). An oxidizing environment would also serve to inhibit Mn and Fe mobility, consistent with bone chemistry, because oxidized species of Mn and Fe are relatively insoluble.

SRS-XRF imaging may also provide clues to how fine-scale soft tissue structure and chemistry may be preserved. The mode of preservation of the *Archaeopteryx* feather distribution has been interpreted previously as resulting from *imprintation*, where bacilliform bacteria colonized the sediment-facing surface of the feathers and promoted early lithification beneath the feathers (34). Once slightly magnified, the iron channel in Fig. 5 (*Center*) is able to pick out individual barbs from the feather. Under ordinary light, the barbs are visible primarily as tiny indentations on the surface of the limestone. This extremely fine detail in the Fe map shows, however, that feather barb patterns are not merely topographic impressions, but that Fe concentrations also follow feather structure.

Although these extremely fine-grained crystals may have been subsequently oxidized postdepositionally, it is reasonable to postulate that reduced sulfur would be released from the feathers as part of the reductive cleavage of disulfide bonds within the cysteine in the barbs and barbules. Under such reducing conditions, mobile ferrous iron within the reactant fluid could readily combine with sulfide to produce precipitates (most probably pyrite) that used the feather fine structure as a template. Bacterial activity, which is the most likely process for feather degradation, controlled by feather structure as postulated (34), may thus be responsible for preferentially depositing the observed Fe-bearing phases.

It is also possible that the Fe patterning seen here is because of original variations in Fe concentration in the feather caused by color banding. Some rod-shaped micron-sized structures have been identified as fossil eumelanosomes in other specimens (33). Iron is present in eumelanin as a chelate, and hence Fe fine structure could perhaps reflect color variation.

Our images are not conclusive because we do not at this time have micron-scale structural information from the same region to compare to the chemical images. However, we interpret the faint Fe zoning presented here as more likely resulting from structural control on secondary precipitates for three reasons:

1. iron patterns are weak,
2. iron is relatively concentrated in the sediment, and
3. the patterns do not repeat with other metals such as Zn that also tend to be present as melanin chelates in soft tissue.

Thus iron zoning in the feathers, in this case, is probably not an original feature of the organism (see Fig. S3 for detailed maps of other elements).

Curation Artifacts. Aspects of the object's curation history also become visible via SRS-XRF. Small (1–2 mm) areas of restoration on several bones are apparent (yellow arrows in Fig. 2; see also Br map Fig. S1K) consistent with previous findings (3), and the Fe image (Fig. S1H) reveals that part of the matrix originated from the reverse side of the specimen. Chlorine distribution (Fig. S1D) reveals handling of the sample in the form of fingerprints along each side of the slab. Such artifacts are typical for exhibited fossils (in *SI Text*, see *Probable Treatment History* for curation details). We note that extreme caution must be exercised in handling, analyzing, and interpreting curated specimens in order to preserve their integrity.

Discussion, Conclusions, and Implications

SRS-XRF shows that P in the rachises and Zn in the bone have been spectacularly conserved in the Thermopolis *Archaeopteryx*, constraining original concentrations and distributions in the living organism. We note that the trace metal Zn imaged in the *Archaeopteryx* bones still remains as an absolutely critical nutrient for the diet of modern birds in captivity (35). Results also indicate that the composition of the surrounding sediment has served to inhibit Ca release but enhance P removal from the bone. Geochemical conditions also likely minimized transfer of Fe and Mn into the bone. Use of fillers and consolidants as well as matrix transfer and surface contamination (fingerprints) may be easily detected by chemical mapping in some cases. The sensitivity, speed, and availability of complementary X-ray techniques all combine to make SRS-XRF imaging a powerful development in the geological and biological sciences. The preservational paradigm that constrains the fossil record can be greatly enhanced by using the SRS-XRF methodology.

Materials and Methods

Thermopolis *Archaeopteryx*. This fossil is reported to have been prepared in the 1970s. Materials used in preparation apparently include a polyester resin as a glue and a bone filler. It is clear that the original fossil bones and the restored portions of the bones have been coated with a consolidant (presumably polyvinyl acetate [PVA], $C_4H_6O_2$). It is also certain that the rest of the rock, feathers included, remains untreated with any consolidant. Techniques used in preparation included the use of a pneumatic or electric chisel to remove the lithographic limestone from the surface of the bones and feathers along natural separations and support a recent preparation date. This "probable treatment" history has been reconstructed as a result of our direct hand lens examination of the fossil. Comparison between filled areas and actual bone shows that the bone consolidant apparently contributes no contaminant elements in the XRF scans, although the filler has measurable Br.

Imaging Details. SRS-XRF imaging was performed at wiggler beam line 6-2 at SSRL. The beam line was operated in its standard configuration with a collimating mirror upstream of a Si (111) monochromator and a pair of total reflection focusing mirrors downstream. For the light element XRF images (Si, P, S, and Cl), the excitation energy was chosen at 3.15 keV; for the heavier element images (Ca, Ba, Mn, Fe, Cu, Zn, Pb, and Br, plus Ni in selected areas), an excitation energy of 13.5 keV was chosen. At low incident energy, the light elements (macronutrients) phosphorous and sulfur were easily resolved. Increasing the incident energy of the beam allowed analysis of heavier elements, especially the transition metals. Because the specimen and the sedimentary matrix are so high in Ca (over 30% by element weight), the second harmonic of the primary beam was of sufficient intensity to also allow mapping of Ca at the lower incident energy. The respective attenuation lengths of the incident X-ray beam in the limestone matrix were approximately 18 μm at 3.15 keV and 200 μm at 13.5 keV. The beam was focused onto a 100 μm diameter, 100 μm thick tantalum pinhole placed at a distance varying for the high energy measurements between 36.35 and 43.65 mm from the fossil surface. Because of the very long focal depth of the setup, the beam striking the sample was only insignificantly larger than the pinhole diameter. The sample was mounted at a 67° angle to the incident beam. A photon-counting single element silicon drift detector (Vortex) combined with Gaussian shaping amplifiers (Canberra) employing 0.125-μs shaping times plus single channel analyzers were used to detect the XRF signals. For each element, the electronic windows were set to capture the fluorescent photons

from the Kα or Lα emission lines. The width of the electronic windows corresponded to typically 200–300 eV per fluorescence line.

For scans at 13.5 keV excitation energy, the detector was placed at a 90° angle to the beam in order to minimize the unwanted scattering signal. For scans at 3.15 keV where the scattering was much smaller, the detector was placed normal to the sample surface. The *Archaeopteryx* Thermopolis fossil was carefully mounted on a computerized *x-y* translational stage, and rapid scans were performed by continuously translating the sample horizontally across the beam. At the end of each line, a vertical step (80 μm/step) was performed, and the horizontal scan direction was reversed. Data were recorded on the fly in both horizontal directions at a rate corresponding to a travel distance of 80 μm per ∼3 ms readout. The beam intensity I_0 was monitored with a He-filled ion chamber upstream of the pinhole. During scanning, small drifts of the beam with respect to the pinhole were corrected periodically.

For the light element XRF imaging, a helium enclosure was placed around the fossil. On the front side of the fossil, it consisted of ∼22 μm thick polyethylene film that touched the detector window and was ∼2 cm from the pinhole. Sample surface to detector distance averaged 20 mm. We found that the polyethylene had a small amount of Zn contamination and therefore ran the high energy XRF imaging without the enclosure. At high energy, in order to reduce the very large Ca signal we furthermore placed a 50.8 μm thick Al foil in front of the detector, which was placed at a distance of 75 mm from the interaction point. Both the air absorption and the Al foil reduced the Ca Kα fluorescence by a factor of 500, whereas the 3d transition metal signals were reduced only by between 20% and 80%.

Elemental Quantification and Point Analyses. Point analyses were completed by driving the rapid scanning stage to a location of interest defined by previously acquired maps, counting for 200 seconds (as compared to the ∼3.3 ms per pixel used in rapid scanning), and acquiring a full energy dispersive spectrum. We note that limits of detection are several atomic weight percent for

low atomic weight elements, decreasing to approximately 1 ppm for heavier elements such as arsenic. We have explicitly attempted to account for the effects of bone consolidant in our calculated elemental concentrations given in Table 1, by including a 25 μm thick PVA layer in our model geometry. However, our imprecise knowledge of the thickness of this PVA film contributes most of our estimated 50% error for the light elements. (See Fig. S4 for a representative point analysis spectrum.)

Concentration profiles were scaled by using point analyses after a preliminary check to see whether point analysis yields were comparable to relative yields produced during scanning. Point analysis counts for each element were integrated over the equivalent energy window used in mapping and then normalized to active counting time. In all cases, point analyses compared well to yields at the same pixel for each element produced during scanning.

XANES Analysis. XANES was recorded in fluorescence mode by scanning the incident beam energy (via monochromator rotation) through the sulfur K edge and recording the emitted intensity of the sulfur Kα line as a function of incident energy. A K_2SO_4 standard was used to calibrate the energy of the monochromator position.

1. von Meyer H (1861) *Archaeopteryx lithographica*. *Neues Jahrbuch für Mineralogie, Geologie und Paläontologie* 1861:678–679.
2. Padian K, de Ricqles A (2009) The origin and evolution of birds: 35 years of progress. *CR Palevol* 8:257–280.
3. Mayr G, Pohl B, Peters DS (2005) A well-preserved *Archaeopteryx* specimen with theropod features. *Science* 310:1483–1486.
4. Mayr G, Pohl B, Hartman S, Peters DS (2007) The tenth skeletal specimen of *Archaeopteryx*. *Zool J Linn Soc-Lond* 149:97–116.
5. Jenkins R (1999) *X-Ray Fluorescence Spectroscopy* (Wiley, New York), 2nd Ed.
6. Reed SJB (2005) *Electron Microprobe Analysis and Scanning Electron Microscopy in Geology* (Cambridge Univ Press, Cambridge, UK), 2nd Ed.
7. Morton RW, Witherspoon KC (1993) Elemental x-ray imaging of fossils. *Adv X Ray Anal* 36:97–104.
8. Havrilla GJ, Morton RW, Miller TC, Huntley KG (2003) Stereoview elemental x-ray imaging. *52nd Annual Denver X-ray Conference Abstracts*, (International Center for Diffraction Data, Newton Square, PA), Vol 212.
9. Horowitz P (1972) Scanning x-ray microscope using synchrotron radiation. *Science* 178:608.
10. Kemner KM, et al. (2004) Elemental and redox analysis of single bacterial cells by x-ray microbeam analysis. *Science* 306:686–687.
11. Bergmann U (2007) Archimedes brought to light. *Phys World* 20:39–42.
12. Wright ME (2005) X-rays illuminate ancient writings. *Nature* 435:257.
13. Service RF (2006) Brilliant x-rays reveal fruits of a brilliant mind. *Science* 313:744.
14. Dik J, et al. (2008) Visualization of a lost painting by Vincent van Gogh using synchrotron radiation based x-ray fluorescence elemental mapping. *Anal Chem* 80:6436–6442.
15. Popescu BFG, et al. (2009) Mapping metals in Parkinson's and normal brain using rapid-scanning x-ray fluorescence. *Phys Med Biol* 54:651–663.
16. Jamtveit B, Wogelius RA, Fraser DG (1993) Zonation patterns of Skarn garnets: Stratigraphic records of hydrothermal systems. *Geology* 21:113–116.
17. Wogelius RA, Fraser DG, Feltham D, Whiteman M (1992) Trace elements in dolomite: Proton microprobe data and constraints on fluid compositions. *Geochim Cosmochim Acta* 56:319–334.
18. Wogelius RA, Fraser DG, Grime GW, Wall GRT (1997) Trace element and isotopic zonation in vein calcite from the Mendip Hills, UK, with spatial-process correlation analysis. *Geochim Cosmochim Acta* 61:2037–2051.
19. Whitaker FF, Smart PL, Vahrenkamp VC, Nicholson H, Wogelius RA (1994) Dolomitisation by near normal sea water? Field evidence from the Bahamas. *Dolomites and Dolomitization*, eds B Purser, M Tucker, and D Zenger (Blackwell, Oxford).
20. Gault AG, et al. (2008) Arsenic in hair and nails of individuals exposed to arsenic-rich groundwaters in Kandal Province, Cambodia. *Sci Total Environ* 393:168–176.
21. Briggs DEG, Kear AJ, Martill DM, Wilby PR (1993) Phosphatization of soft-tissue in experiments and fossils. *J Geol Soc London* 150:1035–1038.
22. European Down and Feather Association. http://www.edfa.eu/englisch/eumwelt.htm. See figure 1 on this Web page. Accessed December 17, 2009.
23. Metcheva R, Yurukova L, Teodorova S, Nikolova E (2006) The penguin feathers as bioindicator of Antartica environmental state. *Sci Total Environ* 362:259–265.
24. Marlow HW, Caldwell MJ (1934) A chemical and x-ray study of "flightless" feathers. *J Hered* 25:265–268.
25. Liu XD, et al. (2006) P and trace metal contents in biomaterials, soils, sediments and plants in colony of red-footed booby (Sula sula) in the Dongdao Island of South China Sea. *Chemosphere* 65:707–715.
26. Kelsall JP, Calaprice JR (1972) Chemical content of waterfowl plumage as a potential diagnostic tool. *J Wildlife Manage* 36:1088–1097.
27. Niecke M, Heid M, Kruger A (1999) Correlations between melanin pigmentation and element concentration in feathers of white-tailed eagles (Haliaeetus albicilla). *J Ornithol* 140:355–362.
28. Pillai P, Archana G (2008) Hide depilation and feather disintegration studies with keratinolytic serine protease from a novel Bacillus subtilis isolate. *Appl Microbiol Biotechnol* 78:643–650.
29. Agusa T, et al. (2005) Body distribution of trace elements in black-tailed gulls from Rishiri Island, Japan: Age-dependent accumulation and transfer to feathers and eggs. *Environ Toxicol Chem* 24:2107–2120.
30. Shinomiya T, et al. (1998) In- and out-flows of elements in bones embedded in reference soils. *Forensic Sci Int* 98:109–118.
31. Goodwin MB, Grant PG, Bench G, Holroyd PA (2007) Elemental composition and diagenetic alteration of dinosaur bone: Distinguishing micron-scale spatial and compositional heterogeneity using PIXE. *Palaeogeogr Palaeocl* 253:458–476.
32. Munnecke A, Westphal H, Kolbl-Ebert M (2008) Diagenesis of plattenkalk: Examples from the Solnhofen area (Upper Jurassic, southern Germany). *Sedimentology* 55:1931–1946.
33. Vinther J, Briggs DEG, Prum RO, Saranathan V (2008) The colour of fossil feathers. *Biol Letters* 4:522–525.
34. Davis PG, Briggs DEG (1995) Fossilization of feathers. *Geology* 23:783–786.
35. Wolf P, Bayer G, Wendler C, Kamphus J (1998) Mineral deficiency in pet birds. *J Anim Physiol An N* 80:140–146.
36. Bausch WM, et al. (1994) Eichstätt and Cerin: Geochemical comparison and definition of two different Plattenkalk types. *Geobios* 16:107–125.

GEOLOGY

EVOLUTION